Novel microstructure-controlled Li ion conductive oxide–based ceramic solid electrolytes supporting high current densities

Nataly Carolina Rosero-Navarro[a*], Haruna Watanabe[b], Randy Jalem[c,d], Shota Sugio[b], Hiroaki Ito[b], Yoshitaka Tateyama[c,d], Akira Miura[a] and Kiyoharu Tadanaga[a]

[a.] Division of Applied Chemistry, Faculty of Engineering, Hokkaido University, Sapporo 060-8628, Japan

[b.] Graduate School of Chemical Sciences and Engineering, Hokkaido University, Sapporo 060-8628, Japan

[c.] Center for Green Research on Energy and Environmental Materials & Global Research Center for Environment and Energy based on Nanomaterials Science (GREEN), National Institute for Materials Science (NIMS), Tsukuba, Japan

[d.] Elements Strategy Initiative for Catalysts & Batteries, Kyoto University, Kyoto, Japan

*E-mail address: rosero@eng.hokudai.ac.jp

Abstract

The fabrication of all-solid-state batteries using lithium metal that can be operated at high current densities (free lithium dendrites) is a recognized worldwide goal. We used a glassy lithium borate (LBO)–based novel microstructure as the grain boundary modifier of a garnet-type solid electrolyte to prevent lithium dendrite formation at high current densities. The relative density (90%) and ionic conductivity (10^{-4} S cm^{-1}) were similar for LBO-modified and non-modified solid electrolytes. LBO in the solid electrolyte microstructure distributes the current homogeneously and prevents dendrite nucleation and propagation, suppressing lithium dendrites up to 10 mA cm^{-2}. Low voltage response (~10 mV) at a current density of 10 mA cm^{-2} for 60 galvanostatic plating–stripping cycles establishes the fast-charging capability of this composite electrolyte.

Batteries are an indispensable energy storage technology in the electrification of vehicles and efficient integration of renewable energy to large-scale energy storage, including solar and wind power. All-solid-state lithium batteries based on solid oxide electrolytes, including garnet-type electrolytes (e.g., $Li_7La_3Zr_2O_{12}$, LLZ), are safe and yield high energy densities due to their electrochemical compatibility with lithium anodes and wide electrochemical potential window. The poor wettability of the solid electrolyte surface against lithium metal (lithiophobicity) has been addressed by employing buffer metallic or inorganic layers.[1-9] For this, a nanometric coating is first applied to the solid electrolyte, and subsequently, the lithium metal is melted on the modified surface at 175–300 °C to form lithium alloys, which ensure adhesion. The adhesion of lithium metal on the LLZ surface modified with thicker inorganic coatings, such as Li_2O and SiO_2, has been reported.[10, 11] They provide sufficient physical contact between lithium metal and the solid electrolyte and significantly reduce the interfacial resistance. However, the limiting current density (or critical current density, CCD), at which the cell is short-circuited due to lithium dendrite formation, is less than 0.9 mA cm^{-2} [9]. The CCD of garnet-type solid electrolytes, which is lower than that of liquid electrolytes based on organic solvents and lithium salts (10 mA cm^{-2}), is not sufficient for fast-charging applications.[12]

The microstructural characteristics of the solid electrolyte, such as pores, cracks, or defects on the surface and inside the solid ceramic electrolyte, promote the formation of lithium dendrites.[13, 14] These defects provide the initial nucleation current, resulting in dendrite growth and cell short (dendrite propagation). Lithium metal preferentially penetrates the solid electrolyte across the grain boundaries. [15-17] This can be addressed using two

approaches: (i) reducing the grain boundaries using high-density electrolytes and (ii) modifying the grain boundaries using additional secondary phases. The high-density electrolytes with fewer grain boundaries improve the CCD owing to the reduced activation energy for total Li-ion migration according to molecular dynamics studies.[18] Lu et al.[19] reported an increase in the CCD of a Li–Al alloy|LLZ interface from 0.2 mA cm^{-2} to 0.7 mA cm^{-2} when the relative density was increased from 90 to 97%. The lithium-rich phases, such as Li_2CO_3/LiOH[20], Li_3PO_4[21], and Li_2ZrO_3[22], along the solid electrolyte microstructure enhance the lithium transport between the grains, making the solid electrolyte more resilient to dendrite formation. Li_2ZrO_3 exhibits an improved relative density and CCD of 95% and 1.4 mA cm^{-2}, respectively. Therefore, tuning the solid electrolyte microstructure can enhance the electrochemical properties of the solid electrolyte and significantly increase the CCD.

We studied the effect of glassy LBO as a grain boundary modifier of the solid electrolyte microstructure to prevent dendrite growth at high current densities. LBO has been widely used as a sintering additive for garnet-type solid electrolytes. It does not react with the solid electrolyte and is present in the sintered ceramic as an amorphous phase in tripe-point grain boundaries.[23] To the best of our knowledge, the impact of sintered, garnet-type LBO solid electrolyte microstructure on CCD has not been reported.

We studied the impact of the solid electrolyte microstructure on CCD using a Ta-doped LLZ solid electrolyte (LLZT) with a similar conductivity (~0.1 mS cm^{-1}) and relative density (90%) when modified with LBO (LLZT-LBO) and in the non-modified (LLZT) form. Li–Au alloy was used as an interlayer to ensure a low interfacial resistance between the solid

electrolyte and lithium metal (experimental details are provided in the Supporting Information).

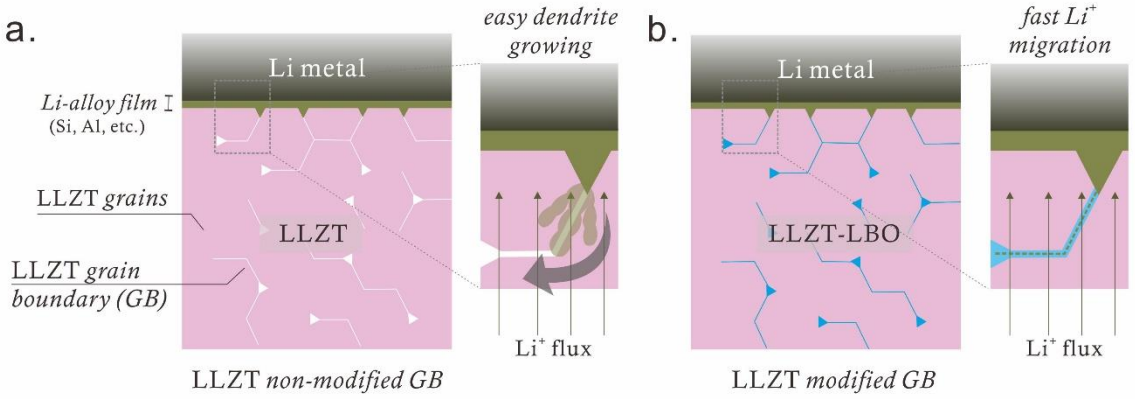

Figure 1. Illustration of dendrite growth during Li plating for a) LLZT and b) LLZT-LBO.

Figure 1 compares the Li plating in pristine LLZT (non-modified grain boundary) and LLZT-LBO (modified grain boundary) at high current densities. While dendrite propagation is facilitated along the grain boundaries (or any defect through the ceramic electrolyte) in pristine LLZT (Figure 1a), a homogeneously distributed current due to LBO in the LLZT-LBO microstructure prevents dendrite nucleation and propagation, suppressing the formation of lithium dendrites. The stability of LLZT and LLZT-LBO after plating and stripping lithium in symmetric cells indicates the absence of interfacial degradation and resistance to short circuits up to 10 mA cm^{-2} for LLZT-LBO. The galvanostatic plating and stripping cycles of lithium at 10 mA cm^{-2} indicate a low voltage response (~10 mV) up to 60 cycles, establishing the fast-charging capability of this composite electrolyte.

Figure 2a and Table 1 summarize the general chemical and electrochemical properties of LLZT and LLZT-LBO. Figure 2a shows the X-ray diffraction (XRD) patterns of LLZT and LLZT-LBO sintered at 1000 °C in comparison to the calcination powder (700 °C), which was used to synthesize the samples. The XRD pattern of the calcined powder corresponds to the standard cubic phase with the $Ia\bar{3}d$ space group (ICSD #183607). Although secondary phases corresponding to lanthanum oxide and lanthanum zirconate were observed in the calcined powder, they disappeared after sintering for the LLZT and LLZT-LBO electrolytes. The lattice parameters of LLZT and LLZT-LBO are 12.93 (3) and 12.93 (6) Å, respectively, which are consistent with the reported values of analogous LLZT garnet-type electrolytes (12.94 Å)[24, 25]. LBO did not react with LLZT grains and was present in the sintered ceramic body as an amorphous phase. [23] The cross-sectional scanning electron microscope (SEM) images (Figures 2b and c) of the LLZT and LLZT-LBO pellets (relative density = ~90%) indicate that the microstructures are similar and contain grains of 1–20 μm with sufficient contact between the grains, which was also confirmed by analyzing the cross-section of the polished surface (Figure S1).

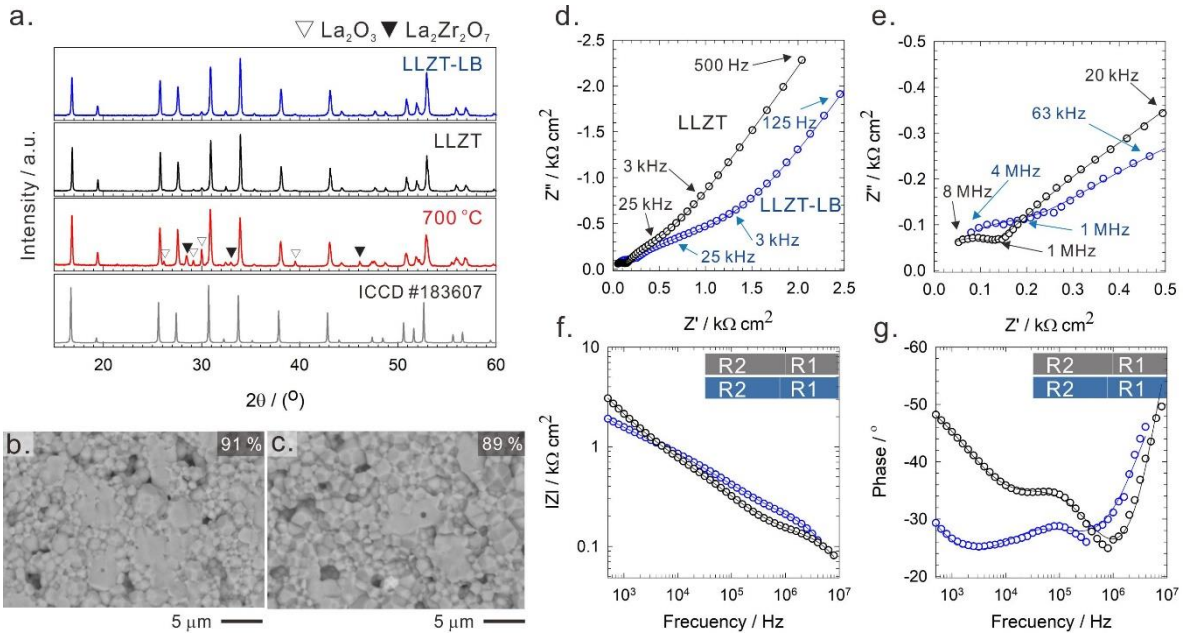

Figure 2. a) XRD patterns of calcination powder (700 °C) and sintered LLZT and LLZT-LBO at 1000 °C. Reference XRD pattern of cubic LLZ phase ICSD #183607 is also included. Cross-sectional SEM images of b) LLZT and c) LLZT-LBO. d–e) Nyquist and f–g) Bode plots of LLZT and LLZT-LBO at 25 °C. Open circles represent the measured data, and solid lines indicate the fit of the data. Information of fitting to the equivalent circuit is provided in Figure S2b.

Table 1. Fitting results of impedance profiles (Figure 2h) of LLZT and LLZT-LBO using equivalent circuits in Figure S3.

Sample	R_1 (Ω cm^2)	σ (R_1) (mS cm^{-1})	R_2 (Ω cm^2)	σ (R_2) (mS cm^{-1})	R_{Total} (Ω cm^2)	σ_{Total} (mS cm^{-1})
LLZT	92.17	0.94	419.59	0.21	511.76	0.17
LLZT-LBO	153.81	0.70	1145.95	0.09	1299.13	0.08

Figures 2d–g show impedance profiles of the LLZT and LLZT-LBO at 25 °C using Au-blocking electrodes. Two semicircles (Figure 2d–e) at high and intermedium frequencies (8–1 MHz and 1–25 kHz, respectively) can be attributed to the resistance of the solid

electrolyte[26, 27], including those from grains (R1 in Figure 3f–g) and grain boundaries (R2 in Figure 3f–g). The tail region at low frequency (approximately 3 Hz) can be attributed to the stainless-steel blocking electrodes (Figure S2a). LLZT-LBO shows a wider semicircle at intermedium frequencies, indicating a higher grain boundary resistance than LLZT because of the less conductive LBO (two orders of magnitude lower than LLZT). Fitting to equivalent circuits (Figure S2b) yields the grain boundary resistance in LLZT and LLZT-LBO (Table 1) as 82% and 88%, respectively. Although we used a simple equivalent, the complex contribution of the resistance components at intermedium frequencies, observed in the phase plot, suggests multiple resistive contributions at high frequencies for the LLZT-LBO. The total ionic conductivities, including that of grain and grain boundary (Table 1), are 0.1 and 0.08 mS cm^{-1} for LLZT and LLZT-LBO, respectively. Both LLZT and LLZT-LBO exhibit similar chemical and electrochemical properties with a slight variation in the ionic conductivity owing to the presence of LBO in the LLZT-LBO.

Figure 3 shows the impedance profiles of the Au-coated LLZT and LLZT-LBO symmetric cells using metallic lithium (as non-blocking electrodes) before (as assembled) and after the heat treatment at 175 °C (lithium melting) to promote the adhesion of lithium metal through the formation of a Li–Au alloy interlayer.

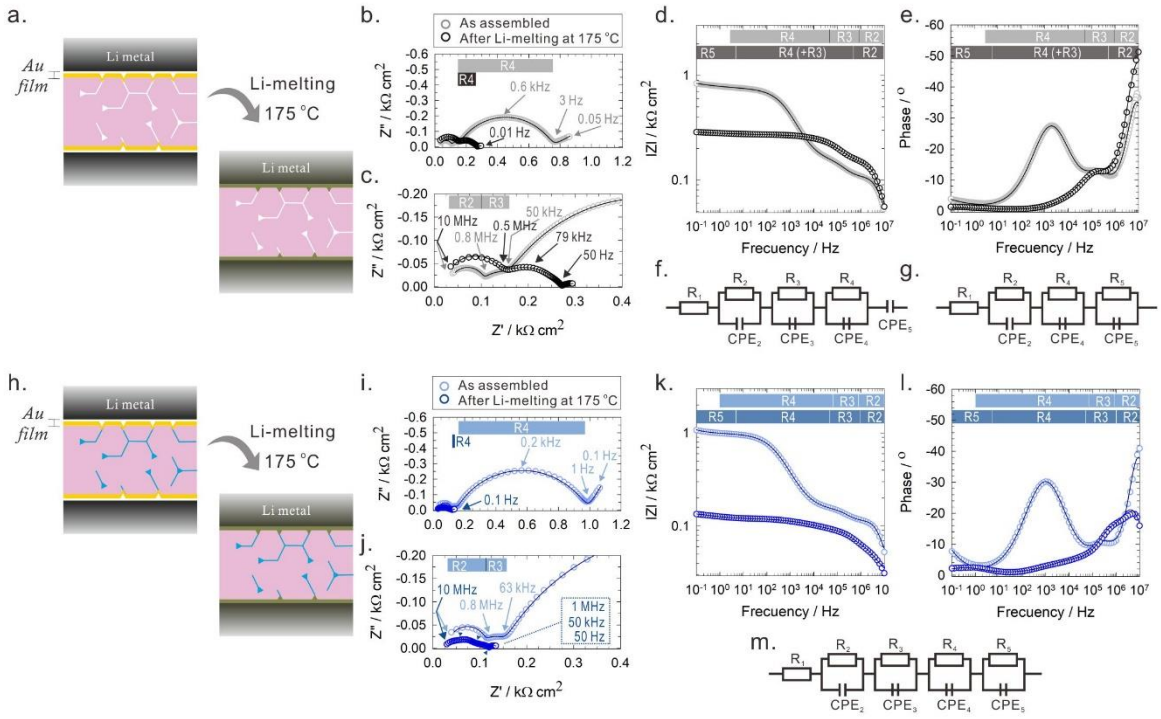

Figure 3. Illustration of LLZT and LLZT-LBO symmetric cells using metallic lithium before (as assembled) and after heat treatment at 175 °C. d–e) Nyquist and f–g) Bode plots of LLZT and LLZT-LBO at 25 °C. m) Equivalent Circuits used to fit the impedance profile of LLZT and LLZT-LBO symmetric cells. Open circles represent the measured data, and solid lines indicate the fit of the data. Information of fitting to the equivalent circuit is provided in Table 2.

Table 2. Fitting results of impedance profiles (Figure 3b–e and 3i–l) of Au-coated LLZT and LLZT-LBO symmetric cells using metallic lithium (as non-blocking electrodes) before (as assembled) and after heat treatment at 175 °C using equivalent circuits in Figures 3f–g and m. The resistances correspond to symmetric cells, and therefore, half of these values correspond to single face resistances.

Resistance components	LLZT	LLZT-175	LLZT-LBO	LLZT-LBO-175
R1 (Ω cm^2)	32.9	23.1	32.9	29.1
R2 (Ω cm^2)	68.6	103.9	76.4	26.2
R3 (Ω cm^2)	45.6	-	36.5	27.5
R4 (Ω cm^2)	595.2	140.8	840.6	37.5
R5 (Ω cm^2)	-	66.7	-	20.7
R total (Ω cm^2)	742.2	334.6	986.4	141.2

Nyquist plots for the Li/LLZT/Li and Li/LLZT-LBO/Li cells before heating exhibit similar profiles (Figures 3b–e and 3i–l), with four resistance components: the interception with the real axis in a high-frequency region (10 MHz, Figures 3c and j), a semicircle in the high-frequency region at 10–0.8 MHz (R_2, Figures 3d–e and 3k–l), and two semicircles in the medium–low-frequency region between 0.8–50/63 Hz (R_3, Figures 3d–e and 3k–l) and 50–3/1 Hz (R_4, Figures 3d–e and 3k–l). Additionally, a small tail region was observed at low frequencies (0.05/0.1 Hz) for both samples. The resistive component at high frequencies is associated with the bulk and grain boundary (R_1 and R_2) resistances of the LLZT and LLZT-LBO pellets, which is consistent with the impedance profiles obtained using Au-blocking electrodes (Figure 2). The resistive components at medium–low frequencies (R_3 and R_4) are associated with the interfacial resistance between LLZT (or LLZT-LBO) and lithium metal and include multiple interfacial resistances, such as LLZT-grain|Au|Li, LLZT-GB|Au|Li, LLZT-grain|Li, and LLZT-GB|Li. The tail observed at low frequencies can be attributed to the charge transfer resistance of the LLZT|Au and LLZT-LBO|Au interfaces.

The impedance profiles were fitted to the equivalent circuit (Figure 3f), in which the constant phase elements (CPEs) were used to simulate the capacitive behavior and the tail at low frequencies. The fitting results are plotted as solid lines in Figures 3b–e and 3i–l and summarized in Table 2. While the resistance values were similar for both cells, R_4 was higher for Li/LLZT-LBO/Li (421 Ω cm^2 for single face) compared to that for Li/LLZT/Li (298 Ω cm^2 for single face) and can be attributed to the high contribution of the grain boundary resistance in the LLZT-LBO solid electrolyte (Figures 2d–g), which affects the interfacial resistance with lithium metal.

After heat treatment at 175 °C, both Li/LLZT/Li and Li/LLZT-LBO/Li cells showed similar profiles (Figures 3b–e and 3i–l) with a slight shift in the contribution of the four resistive components towards the high-frequency region. The partial semicircle at the low frequency (instead of the capacitive tail for the non-heated cells) can be attributed to the formation of the Li–Au alloy. The reduced resistances in the medium–low-frequency region can be attributed to the reduction of the interfacial resistance, which enhanced the contact between the solid electrolyte and lithium metal through the Li–Au alloy. The impedance profiles of Li/LLZT/Li and Li/LLZT-LBO/Li cells after heat treatment were fitted to the equivalent circuits shown in Figures 3g and m, respectively. The equivalent circuit for the Li/LLZT/Li cell impedance profile contains three R||CPE components instead of four, owing to the error in fitting due to the limited information in the associated frequency region. This implies that R_2 might also contain the contribution from R_3.

The interfacial resistances of Li/LLZT/Li (R_4) and Li/LLZT-LBO/Li ($R_3 + R_4$) cells were 70 and 31 Ω cm^2 (for single face), respectively, and are similar to that for the interface between a garnet-type solid electrolyte and Li–Au alloy (~50 Ω cm^2)[7]. The Li/LLZT-LBO/Li cell exhibited reduced interfacial resistance because of the enhanced wettability of LBO against metallic lithium,[10] yielding a reduced value of R_2 (GB) in this cell.

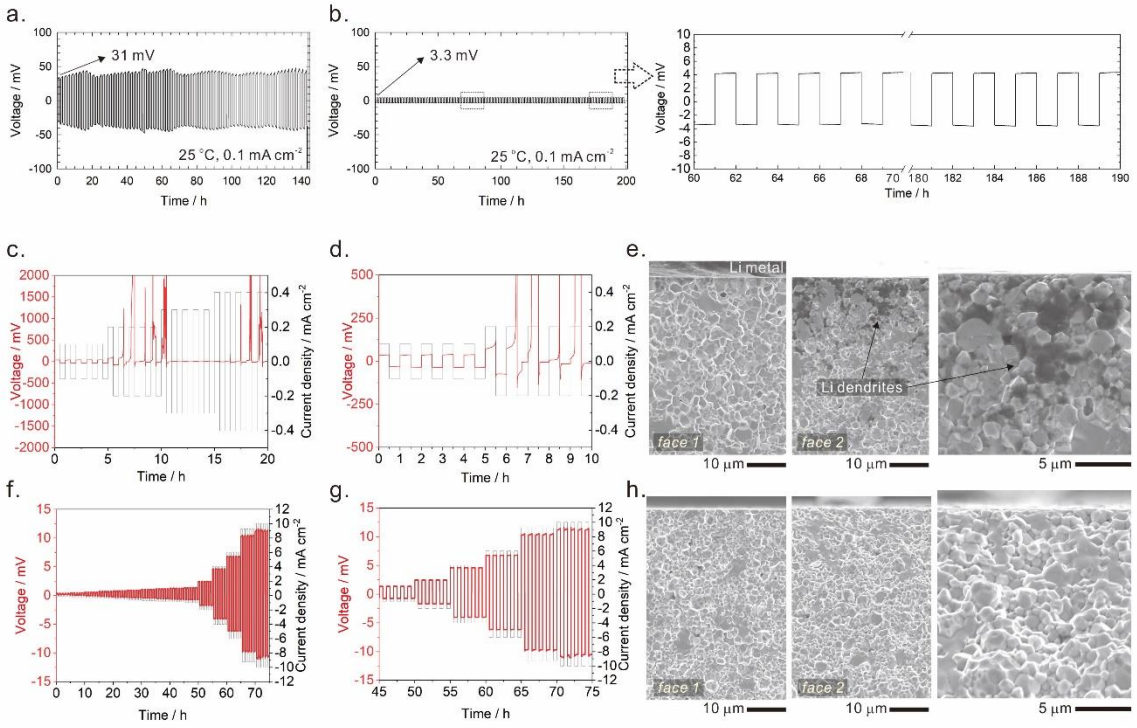

Figure 4. Direct current cycling measurement of a) Li/LLZT/Li and b) Li/LLZT-LBO/Li cells at 0.1 mA cm^{-2}. c–d) and f–g) DC cycling measurements of Li/LLZT/Li and Li/LLZT-LBO/Li cells at different current densities. e and h) cross-sectional SEM images of the LLZT and LLZT-LBO pellets after DC cycling measurement.

The interfacial stabilities of the Li/LLZT/Li and Li/LLZT-LBO/Li cells were studied using a direct current cycling measurement at a constant current density of 0.1 mA cm^{-2}, a typical CCD value for Li–Au alloys[28] (Figure 4). Each galvanostatic step was performed for 60 min and the ohmic interfacial resistances, excluding the internal resistances of the solid electrolyte (half of R_1 + R_2, Table 2), were 247 Ω cm^2 and 5 Ω cm^2 for Li/LLZT/Li and Li/LLZT-LBO/Li cells in their first cycle, respectively. The variation in the interfacial

resistances obtained using impedance and galvanostatic measurements can be attributed to the enhanced interfacial resistance during the lithium dissolution and deposition processes of the Li/LLZT-LBO/Li cell, thereby making the interfacial resistance insignificant. Contrastingly, the interfacial resistance of the Li/LLZT/Li cell increased during the lithium dissolution and deposition processes, indicating an unstable current distribution which increased the interfacial resistance. While the Li/LLZT/Li cell exhibited dendrite short-circuits after 70 cycles (high overpotential ≥ 1 V), the Li/LLZT-LBO/Li cell remained stable with an insignificant change in interfacial resistance up to 100 cycles.

Galvanostatic cycling was performed at different current densities to determine the CCD. Figures 4c–d and f–g illustrate the DC cycling of the Li/LLZT/Li and Li/LLZT-LBO/Li cells at current densities of 0.1–0 mA cm^{-2}. While the large and unstable voltage profile for the Li/LLZT/Li cell (Figures 4c–d) indicates an overpotential (~2 V) at 0.2 mA cm^{-2}, the voltage profile was stable up to 10 mA cm^{-2} for the Li/LLZT-LBO/Li cell (Figures 4f–g) and remained below 15 mV during the test.

After the galvanostatic cycling, the cross-sections of the LLZT and LLZT-LBO pellets were analyzed using SEM, on both faces, (Figures 4e, 4h, S3, S4) and synchrotron XRD (supporting information) to study the changes in the microstructure and crystal phase, respectively. The dark region on the second face corresponds to Li plating (Figure 4e), and the low magnification image (Figure S3a) indicates a 15–20 μm thick deposit of lithium on the surface of the pellet. This was further confirmed by the SEM–energy dispersive X-ray spectroscopy (EDS) analysis (Figure S4). Contrastingly, the low magnification cross-

sectional images for the faces of the LLZT-LBO pellet (Figure 4h) and the surface (Figures S3b and S5) show a clear surface without interface damage, confirming the stability of the LLZT-LBO microstructure at high current densities. The crystal phases of LLZT and LLZT-LBO remained unchanged after galvanostatic measurements (Supporting Information). The DC cycling measurement of a Li/LLZT-LBO/Li cell at a constant current density of 10 mA cm^{-2} (Figure S6) exhibits a low voltage response (~10 mV) up to 60 cycles with a few overpotentials below 50 mV.

Density functional theory (DFT) calculations of the Li/LBO interface were compared with those of the Li/LLZ, as a function of potential (vs. Li/Li^{+}), to elucidate the electrochemical stability caused by LBO in the solid electrolyte microstructure (Figure 5). The formation of the stable phases is studied. While the garnet-type solid electrolyte decomposed electrochemically at potentials higher than 2.9 V, yielding non-conductive phases, such as $La_2Zr_2O_7$ and La_2O_3, LBO remained electrochemically stable up to 3.4 V. This indicated that the electrochemical performance of the solid electrolyte should not be affected by the LBO at high potential and yield high electrochemical stability. At low potentials (0–0.05 V), non-conductive phases, such as La_2O_3, and elastically stiff compounds, such as Zr_4O and Zr_3O (oxo clusters[29]), were formed at the Li/LLZ interface. Contrastingly, Li-containing oxide and borate phases, such as Li_2O and Li–B, were formed at the Li/LBO interface between 0 and 0.043 V, which improved the transport properties at the lithium–metal interface.[10]

The presence of non-conductive phases (LLZ) is critical for current nucleation and dendrite growth[10], and incorporating LBO into the solid electrolyte is expected to improve the electrochemical stability of the solid electrolyte at low potentials, since the LBO inhibits the effects of the non-conductive phases formed from the LLZ. Additionally, the LBO could also be forming a chemical barrier because of its orientation along the grain boundaries and is in direct contact with lithium metal instead of LLZ grains.

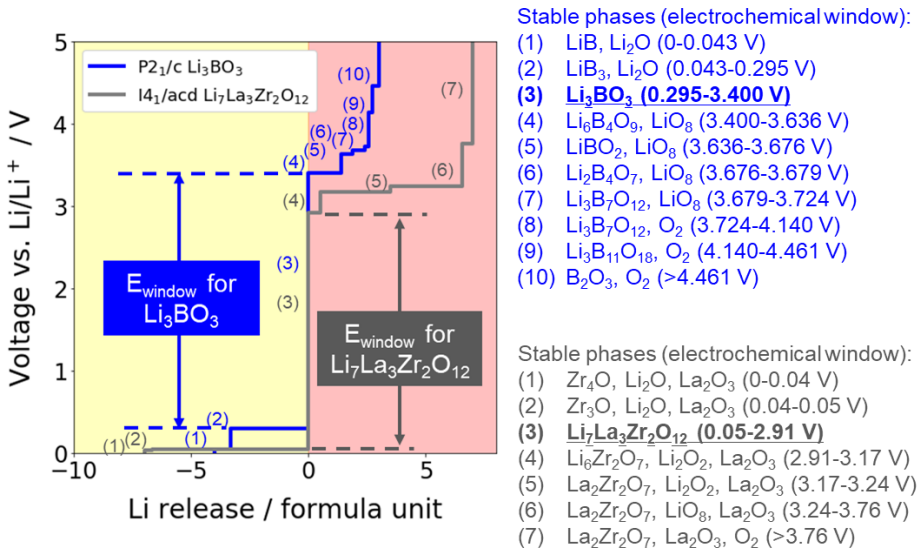

Figure 5. Li grand potential phase stability plots for $P2_1/c$ Li_3BO_3 and garnet $I4_1/acd$ $Li_7La_3Zr_2O_{12}$.

The Li^+ ion migration energies, calculated using DFT (Figure S7), within the LBO crystal structure exhibit low diffusion barriers in the structure (0.13–0.22 eV), indicating fast Li-ion transport. This is significant because LBO is used as a grain boundary modifier for the solid

electrolyte, which exhibits bulk Li^+ ion activation energies of 0.3–0.33 eV[25] and explains the lithium migration at high current densities on account of the LBO.

The designed microstructure of the solid electrolytes plays a critical role in governing the electrochemical properties, particularly the CCD. LBO is an efficient grain boundary modifier of garnet-type solid electrolytes that yields a homogeneous current distribution at high current densities, facilitating the stable lithium dissolution and precipitation at 10 mA cm^{-2} and establishing the fast-charging capabilities of the LLZT-LBO electrolyte. We envisage that the current alternative can be extended to other solid electrolytes.

Acknowledgements

N.C.R.-N. acknowledges financial support by Nippon Sheet Glass Foundation in FY2021. The SEM analysis was carried out with JIB4600F at the "Joint-use Facilities: Laboratory of Nano-Micro Material Analysis", Hokkaido University, supported by "Material Analysis and Structure Analysis Open Unit (MASAOU)". The authors thank Mr. Keita Suzuki for his assistance with cross-section preparation of ceramic electrolytes. Authors thanks the data reproducibility by students of Laboratory of Inorganic Synthesis Chemistry at Hokkaido University during starting-up training 2021.

References

1. W. Luo, Y. Gong, Y. Zhu, K. K. Fu, J. Dai, S. D. Lacey, C. Wang, B. Liu, X. Han, Y. Mo, E. D. Wachsman and L. Hu, *Journal of the American Chemical Society*, 2016, **138**, 12258-12262.
2. X. Han, Y. Gong, K. Fu, X. He, G. T. Hitz, J. Dai, A. Pearse, B. Liu, H. Wang, G. Rubloff, Y. Mo, V. Thangadurai, E. D. Wachsman and L. Hu, *Nature Materials*, 2016, **16**, 572.
3. W. Luo, Y. Gong, Y. Zhu, Y. Li, Y. Yao, Y. Zhang, K. Fu, G. Pastel, C.-F. Lin, Y. Mo, E. D. Wachsman and L. Hu, *Advanced Materials (Weinheim, Germany)*, 2017, **29**, 1606042.
4. C. Wang, Y. Gong, B. Liu, K. Fu, Y. Yao, E. Hitz, Y. Li, J. Dai, S. Xu, W. Luo, E. D. Wachsman and L. Hu, *Nano Letters*, 2017, **17**, 565-571.
5. K. Fu, Y. Gong, B. Liu, Y. Zhu, S. Xu, Y. Yao, W. Luo, C. Wang, S. D. Lacey, J. Dai, Y. Chen, Y. Mo, E. Wachsman and L. Hu, *Science Advances*, 2017, **3**, e1601659.
6. K. Fu, Y. Gong, Z. Fu, H. Xie, Y. Yao, B. Liu, M. Carter, E. Wachsman and L. Hu, *Angewandte Chemie International Edition*, 2017, **56**, 14942-14947.
7. G. V. Alexander, S. Patra, S. V. Sobhan Raj, M. K. Sugumar, M. M. Ud Din and R. Murugan, *Journal of Power Sources*, 2018, **396**, 764-773.
8. M. He, Z. Cui, C. Chen, Y. Li and X. Guo, *Journal of Materials Chemistry A*, 2018, **6**, 11463-11470.
9. A. J. Samson, K. Hofstetter, S. Bag and V. Thangadurai, *Energy & Environmental Science*, 2019, **12**, 2957-2975.
10. N. C. Rosero-Navarro, R. Kajiura, R. Jalem, Y. Tateyama, A. Miura and K. Tadanaga, *ACS Applied Energy Materials*, 2020, **3**, 5533-5541.
11. N. C. Rosero-Navarro, R. Kajiura, A. Miura and K. Tadanaga, *ACS Applied Energy Materials*, 2020, **3**, 11260-11268.
12. F. Han, A. S. Westover, J. Yue, X. Fan, F. Wang, M. Chi, D. N. Leonard, N. J. Dudney, H. Wang and C. Wang, *Nature Energy*, 2019, **4**, 187-196.
13. J. Liu, H. Yuan, H. Liu, C.-Z. Zhao, Y. Lu, X.-B. Cheng, J.-Q. Huang and Q. Zhang, *Advanced Energy Materials*, **n/a**, 2100748.
14. H. Liu, X.-B. Cheng, J.-Q. Huang, H. Yuan, Y. Lu, C. Yan, G.-L. Zhu, R. Xu, C.-Z. Zhao, L.-P. Hou, C. He, S. Kaskel and Q. Zhang, *ACS Energy Letters*, 2020, **5**, 833-843.
15. E. J. Cheng, A. Sharafi and J. Sakamoto, *Electrochimica Acta*, 2017, **223**, 85-91.
16. T. Krauskopf, R. Dippel, H. Hartmann, K. Peppler, B. Mogwitz, F. H. Richter, W. G. Zeier and J. Janek, *Joule*, 2019, **3**, 2030-2049.

17. S. Kim, C. Jung, H. Kim, K. E. Thomas-Alyea, G. Yoon, B. Kim, M. E. Badding, Z. Song, J. Chang, J. Kim, D. Im and K. Kang, *Advanced Energy Materials*, 2020, **10**, 1903993.

18. S. Yu and D. J. Siegel, *Chemistry of Materials*, 2017, **29**, 9639-9647.

19. Y. Lu, X. Huang, Y. Ruan, Q. Wang, R. Kun, J. Yang and Z. Wen, *Journal of Materials Chemistry A*, 2018, **6**, 18853-18858.

20. R. Hongahally Basappa, T. Ito, T. Morimura, R. Bekarevich, K. Mitsuishi and H. Yamada, *Journal of Power Sources*, 2017, **363**, 145-152.

21. B. Xu, W. Li, H. Duan, H. Wang, Y. Guo, H. Li and H. Liu, *Journal of Power Sources*, 2017, **354**, 68-73.

22. C. Zheng, Y. Ruan, J. Su, Z. Song, T. Xiu, J. Jin, M. E. Badding and Z. Wen, *Chemical Engineering Journal (Lausanne)*, 2021, **411**, 128508.

23. N. C. Rosero-Navarro and K. Tadanaga, in *Solid Electrolytes for Advanced Applications*, eds. M. R. and W. W., Springer International Publishing, Cham, 2019, DOI: 10.1007/978-3-030-31581-8_5, pp. 111-128.

24. V. Thangadurai, S. Narayanan and D. Pinzaru, *Chemical Society Reviews*, 2014, **43**, 4714-4727.

25. S. Ramakumar, C. Deviannapoorani, L. Dhivya, L. S. Shankar and R. Murugan, *Progress in Materials Science*, 2017, **88**, 325-411.

26. W. E. Tenhaeff, E. Rangasamy, Y. Wang, A. P. Sokolov, J. Wolfenstine, J. Sakamoto and N. J. Dudney, *ChemElectroChem*, 2014, **1**, 375-378.

27. S. Ohta, J. Seki, Y. Yagi, Y. Kihira, T. Tani and T. Asaoka, *Journal of Power Sources*, 2014, **265**, 40-44.

28. J. Wakasugi, H. Munakata and K. Kanamura, *Journal of the Electrochemical Society*, 2017, **164**, A1022-A1025.

29. P. Walther, M. Puchberger, F. R. Kogler, K. Schwarz and U. Schubert, *Physical Chemistry Chemical Physics*, 2009, **11**, 3640-3647.